

Analyses of Laser Propagation Noises for TianQin Gravitational Wave Observatory Based on the Global Magnetosphere MHD Simulations

WEI SU (苏威),¹ YAN WANG (王炎),¹ CHEN ZHOU (周晨),² LINGFENG LU,³ ZE-BING ZHOU (周泽兵),¹ T.M. LI (李汤姆),^{4,5}
TONG SHI (施通),⁶ XIN-CHUN HU (胡新春),¹ MING-YUE ZHOU (周明越),¹ MING WANG (王明),⁷ HSIEN-CHI YEH,⁸
HAN WANG,^{1,8} AND P.F. CHEN (陈鹏飞)^{4,5}

¹MOE Key Laboratory of Fundamental Physical Quantities Measurements, Hubei Key Laboratory of Gravitation and Quantum Physics, PGMF, Department of Astronomy, and School of Physics, Huazhong University of Science and Technology, Wuhan 430074, China

²Department of Space Physics, School of Electronic Information, Wuhan University, Wuhan 430072, China

³Southwestern Institute of Physics, Chengdu 610041, China

⁴School of Astronomy and Space Science, Nanjing University, Nanjing 210023, China

⁵Key Laboratory of Modern Astronomy & Astrophysics, Nanjing University, China

⁶Department of Climate and Space Sciences and Engineering, University of Michigan, Ann Arbor, MI 48109, USA

⁷Institute of Space Weather, School of Mathematics and Statistics, Nanjing University of Information Science and Technology, Nanjing 210044, China

⁸TianQin Research Center for Gravitational Physics & School of Physics and Astronomy, Sun Yat-sen University, Zhuhai 519082, China

ABSTRACT

TianQin is a proposed space-borne gravitational wave (GW) observatory composed of three identical satellites orbiting around the geocenter with a radius of 10^5 km. It aims at detecting GWs in the frequency range of 0.1 mHz – 1 Hz. The detection of GW relies on the high precision measurement of optical path length at 10^{-12} m level. The dispersion of space plasma can lead to the optical path difference (OPD, Δl) along the propagation of laser beams between any pair of satellites. Here, we study the OPD noises for TianQin. The Space Weather Modeling Framework is used to simulate the interaction between the Earth magnetosphere and solar wind. From the simulations, we extract the magnetic field and plasma parameters on the orbits of TianQin at four relative positions of the satellite constellation in the Earth magnetosphere. We calculate the OPD noise for single link, Michelson combination, and Time-Delay Interferometry (TDI) combinations (α and X). For single link and Michelson interferometer, the maxima of $|\Delta l|$ are on the order of 1 pm. For the TDI combinations, these can be suppressed to about 0.004 and 0.008 pm for α and X . The OPD noise of the Michelson combination is colored in the concerned frequency range; while the ones for the TDI combinations are approximately white. Furthermore, we calculate the ratio of the equivalent strain of the OPD noise to that of TQ, and find that the OPD noises for the TDI combinations can be neglected in the most sensitive frequency range of TQ.

Keywords: plasmas, gravitational waves, Sun: solar wind

1. INTRODUCTION

The first direct detection of gravitational waves (GWs) by the advanced Laser Interferometer Gravitational-Wave Observatory (LIGO) opens up the era of the GW astronomy (Abbott et al. 2016). So far, more than fifty GW events generated by the coalescences of stellar-mass black hole binaries and double neutron stars have been detected by the advanced LIGO and advance Virgo (Abbott et al. 2019, 2020). The underground and cryogenic detector KAGRA (Somiya 2012) has recently started joint observations with the advanced LIGO and advance Virgo. Due to the terrestrial noises, the ground-based detectors are most sensitive to the GW signals in the acoustic band ($\gtrsim 10$ Hz).

Several space-borne missions, e.g., LISA (Amaro-Seoane et al. 2017), TianQin (TQ; Luo et al. 2016), Taiji (ALIA descoped; Gong et al. 2015), ASTROD-GW (Ni 1998), gLISA (Tinto et al. 2015), BBO (Cutler & Harms 2006) and

Corresponding author: Wang Y., Zhou C., Lu L.

ywang12@hust.edu.cn, chenzhou@whu.edu.cn, lulingfeng@swip.ac.cn

DECIGO (Kawamura et al. 2011), have been proposed to explore the abundant GWs sources in the mHz band, which can be used to deepen our understandings in fundamental physics, astrophysics and cosmology.

Both LISA and TQ are in nearly equilateral triangular constellations which are formed by three drag-free satellites interconnected by infrared laser beams. The heterodyne transponder-type laser interferometers are used to measure the relative displacements of the test masses (TMs) with the accuracy of 10^{-12} m/Hz^{1/2} in mHz. This constellation forms up to three Michelson-type interferometers. Different from LISA, TQ's satellites will be deployed in a geocentric orbit with an altitude of 10^5 km from the geocenter and the distances between each pair of satellites $\approx 1.7 \times 10^5$ km (Luo et al. 2016). The detector's plane formed by three satellites is optimized to detect the continuous GW signals from the candidate ultracompact white-dwarf binary RX J0806.3+1527 (Israel et al. 2002). Currently, both science cases (Feng et al. 2019; Wang et al. 2019; Shi et al. 2019; Bao et al. 2019; Liu et al. 2020; Fan et al. 2020; Huang et al. 2020) and technological realizations (Luo et al. 2020; Ye et al. 2019; Tan et al. 2020; Yang et al. 2020; Su et al. 2020; Lu et al. 2020) have been under intensive investigations for TQ. A brief summary of TQ's recent progress can be found in Mei et al. (2020).

The space plasma contributes as one of the main sources of environmental noises for space-borne GW detectors. For example, when the laser beams propagate in the space plasma the dispersion effect can lead to time delay and optical path difference (OPD) between different beams and produce additional noise for the relative displacement measurement. Since the plasma frequency ω_p in the space environment is much larger than the electron gyrofrequency, OPD is mainly caused by the total electron content (TEC) along each laser beam (Lu et al. 2021). Moreover, the space magnetic field can induce the time variation of the polarization of electromagnetic (EM) waves, and the interaction between the space magnetic field and the test masses can generate additional non-conservative forces on the test masses (Hanson et al. 2003; Schumaker 2003; Su et al. 2020; Armano et al. 2020).

Space environment parameters, e.g., the magnetic field and density, vary significantly in time and space (Su et al. 2016; Wang et al. 2018), which can be categorized, in descending characteristic sizes, into three spatial scales: global scale, magnetohydrodynamic (MHD) scale, and plasma scale. In the global scale, the solar wind interacts with the Earth's magnetic dipole field to form structures such as bow shocks, magnetosheath, magnetopause, magnetotail, etc. (Lu et al. 2015; Wang et al. 2016). The density and magnetic field in different structures are essentially different. As the satellites orbiting around the Earth, the laser beam between two satellites passes through different structures, thus the OPD caused by the space plasma will be a function of time. Furthermore, because the solar wind is changing continually, the shapes and properties (e.g., the magnetic field and density) of these structures are also evolving. In the MHD scale, instabilities, such as Kelvin-Helmholtz (K-H) instability, can cause variations of density and magnetic field at the magnetosphere boundary layer (Hasegawa et al. 2004). In the plasma scale, plasma waves, such as electromagnetic ion cyclotron (EMIC) waves (Allen et al. 2015), ultra-low-frequency (ULF) waves (Soucek et al. 2015; Takahashi et al. 2018), kinetic Alfvén waves (KAWs) (Zhao et al. 2014), etc., are widely found in the solar wind, magnetosheath, and magnetosphere. Turbulence exists at sizes ranging from MHD to plasma scales (He et al. 2012; Sahraoui et al. 2013; Huang et al. 2018). Besides, eruption events from the Sun (e.g., coronal mass ejections, and coronal shocks, Su et al. 2015, 2016) and Earth magnetosphere (e.g., magnetic reconnections, Huang et al. 2012; Takahashi et al. 2018; Zhou et al. 2019) can lead to variations of density and magnetic field in multiple scales. In this work, we evaluate the effect of the OPD noise rooted from the space plasma at the global and MHD scales on the detection of GWs for TQ.

This paper is organized as follows. The theory of EM wave propagation in space plasma is briefly summarized in Section 2. In Section 3, we introduce the MHD model, i.e., the Space Weather Modeling Framework (SWMF; Tóth et al. 2005), which is adopted in this work. The calculation and results of the OPD noise are presented in Section 4. Section 5 discusses the impact of our work on the detection of GWs for TQ. Our paper is concluded in Section 6.

2. ELECTROMAGNETIC WAVE PROPAGATION IN SPACE PLASMA

For a train of EM waves with a frequency f (angular frequency ω) propagating in the cold magnetized plasma of the Earth magnetosphere and solar wind, the refractive index μ can be described by the Appleton-Hartree (A-H) equation (Hutchinson 2002):

$$\mu^2 = 1 - \frac{X}{1 - iZ - \frac{Y^2}{2(1-X-iZ)} \pm \sqrt{Y_L^2 + \frac{Y^4}{4(1-X-iZ)^2}}}, \quad (1)$$

where i represents the imaginary unit, X , Y , and Z are defined as:

$$X = \frac{\omega_p^2}{\omega^2}, \quad Y = \frac{\omega_B}{\omega}, \quad Z = \frac{\nu}{\omega}. \quad (2)$$

Here ω_p , ω_B and ν are the plasma frequency, gyrofrequency, and electron collision frequency, respectively:

$$\omega_p^2 = \frac{e^2 N}{m \varepsilon_0}, \quad \omega_B = \frac{eB}{m}, \quad (3)$$

where m is the electron mass, e is the elementary charge, N is the electron number density, ε_0 is the vacuum electric permittivity, and B is the background magnetic field strength. In Equation (1), $Y_T = Y \cos \theta$ and $Y_L = Y \sin \theta$, where θ is the angle between the propagation direction of the EM wave and the direction of the background magnetic field.

Since the electron collision frequency ν of the plasma in the magnetosphere and solar wind are on the order of 10^{-9} s^{-1} , which are much lower than the frequency of the diode-pumped Nd:YAG laser ($\approx 2.8 \times 10^{14} \text{ s}^{-1}$) used for TQ, the space plasma can be considered as collisionless. Thus, Z can be ignored. Besides, take the typical electron number density to be 5 cm^{-3} and the typical magnetic strength to be 5 nT at the geocentric distance of 10^5 km , ω_p and ω_B in the magnetosphere and solar wind are on the order of 10^5 rad s^{-1} and 10^3 rad s^{-1} , respectively, both are much lower than ω . Therefore, Equation (1) can be simplified as,

$$\mu^2 = 1 - X. \quad (4)$$

The group refractive index μ_g can be deduced as:

$$\mu_g = \frac{\partial(\mu\omega)}{\partial\omega} = \frac{\partial\omega\sqrt{1-X}}{\partial\omega} = \frac{2\omega}{2\sqrt{\omega^2 - \omega_p^2}} = \frac{1}{\sqrt{1-X}} = \frac{1}{\mu} \approx 1 + \frac{X}{2} = 1 + \frac{KN}{2f^2}, \quad (5)$$

where $K = e^2/(4\pi^2 m \varepsilon_0) = 80.6 \text{ m}^3 \text{ s}^{-2}$.

The time (τ) that takes EM waves propagating a distance of L in space plasma is:

$$\tau = \int_L \frac{ds}{v_g} = \int_L \frac{ds}{c/\mu_g}, \quad (6)$$

where c is the speed of light in vacuum, $L \approx 1.7 \times 10^8 \text{ m}$ for TQ. The time delay ($\Delta\tau$) relative to the vacuum case is:

$$\Delta\tau = \frac{1}{c} \int_L \left(1 + \frac{KN}{2f^2}\right) ds - \frac{L}{c} = \frac{K}{2cf^2} \int_L N ds. \quad (7)$$

Here, $\int_L N ds$ is called TEC. According to Equation (7), the OPD can be calculated as:

$$\Delta l = c\Delta\tau = \frac{K}{2f^2} \int_L N ds. \quad (8)$$

Equation (8) shows that the OPD noise Δl of a single arm between two satellites is determined by the integrated electron number density along the laser link.

3. MHD SIMULATION

According to Section 2, in order to study the OPD noise for TQ, we need to obtain the distributions of the electron number density in the vicinity of the laser links in Figure 2 (see also Figure 1 in Su et al. (2020)), which requires the global MHD simulations of the Earth magnetosphere. In this work, we adopt the Space Weather Modeling Framework (SWMF) to simulate the interaction between the solar wind and the Earth magnetosphere (Tóth et al. 2005). SWMF has been thoroughly validated in the study of the Earth magnetosphere (Zhang et al. 2007; Welling & Ridley 2010; Dimmock & Nykyri 2013), and it has been used widely (Lu et al. 2015; Wang et al. 2016; Takahashi et al. 2018). The simulation can be requested on the Community Coordinated Modeling Center (CCMC), which is done by the SWMF/Block-Adaptive-Tree-Solarwind-Roe-Upwind-Scheme (BATSUS).

The real time solar wind parameters observed by the Advanced Composition Explorer (ACE; Stone et al. 1998) are taken as the simulation inputs, which include the ion number density n_i , z component of magnetic field B_z , and solar wind dynamic pressure P_{dyn} as illustrated by Figure 1. The time range of the inputs is from 2008-05-01 00:00 UT to 2008-05-04 24:00 UT with a temporal resolution of 1 min. The input data are the same as in Su et al. (2020). The ranges of the Geocentric Solar Magnetospheric (GSM) coordinates in the simulation domain are $-250R_E < x < 33R_E$

(R_E , the radius of the Earth), $|y|$ and $|z| < 48R_E$, which contain the solar wind in the interplanetary space, the bow shock, magnetopause and magnetotail of the Earth. In the region where $|x|, |y|, |z| < 20R_E$, the vicinity of the dayside magnetopause and the near-tail has the finest resolution of $0.25R_E$, the resolution of the rest region is $0.5R_E$. The output parameters of the simulation contain the magnetic field (B_x, B_y, B_z), the plasma parameters (e.g., bulk flow velocity v_x, v_y, v_z , number density of ions n_i , pressure P), and electric current (J_x, J_y, J_z). The output parameters in the GSM coordinates are converted to the Geocentric Solar Ecliptic (GSE) coordinates in the following calculation. Generally, the plasma in the solar wind and magnetosphere is quasi-neutral at the MHD scale, and the number densities of electrons and ions n_i are approximately equal. This has been confirmed by several observations (Zhang et al. 2007; Welling & Ridley 2010). Therefore, we simply use n_i outputted from the simulation as electrons number density in the calculation of the OPD noise.

In the GSE coordinates, we define the intersection angle between the Sun-Earth vector and the projection of the normal of the detector plane on the ecliptic plane as ϕ_s , which shows an annual variation from 0° to 360° (Su et al. 2020) and is equal to 120.5° at the spring equinox (Hu et al. 2018). In order to describe the relative position of the geometric structure of the Earth magnetosphere and the TQ's constellation conveniently, ϕ_s is transformed to its corresponding acute angle φ_s hereafter. φ_s can be approximately regarded as a constant during one orbit period of the TQ satellite around the Earth (3.65 days, Su et al. 2020). In the following sections, we focus on the OPD noises at four typical positions with $\varphi_s = 0^\circ, 30^\circ, 60^\circ$, and 90° .

4. RESULTS

4.1. Laser links in magnetosphere and OPD noise

Taking the simulation at 2008-05-03 20:00 UT as an example, the electron number density distributions on the detector's planes (at $\varphi_s = 0^\circ, 30^\circ, 60^\circ, 90^\circ$) are shown on the left columns of Figure 2, in which ξ is the intersection line between the orbit plane and the ecliptic plane, and ζ is along the intersection of the detector's plane and a plane perpendicular to ξ . ζ is approximately vertical to the ecliptic plane since the angle between the ecliptic plane and the normal of the detector's plane is only 4.7° (Hu et al. 2018). The Earth magnetosheath is the downstream of the bow shock, therefore its electron number density is higher than the ones in the solar wind and the magnetosphere. As shown in Figure 2, the boundary of the magnetosheath on the sunside and earthside are the bow shock and magnetopause, respectively. The geometric structures of the magnetosphere on the four detector's planes are different. For $\varphi_s = 90^\circ$, the nose of the bow shock is located at $\xi \approx 10 R_E$ measured from the geocenter. For $\varphi_s = 0^\circ$, the magnetopause and bow shock are approximately circular and they are located at $\approx 15 R_E$ and $\gtrsim 20 R_E$, respectively.

With the time-varying positions of three TQ's satellites (S1, S2, and S3), the laser links can be obtained. In Figure 2, the laser links S1-S2, S2-S3, and S3-S1 are represented as blue, orange, and green lines, respectively. Note that the initial position of S1 is located at $\xi = 15.7 R_E$ and $\zeta = 0 R_E$. For $\varphi_s = 60^\circ$ and 90° , S1-S2 and S3-S1 will pass through the solar wind, bow shock, magnetosheath, magnetopause and magnetosphere; While S2-S3 that passes through the magnetotail is almost enclosed in the magnetosphere. We obtain the number density distributions along these three laser links, shown in the corresponding colors in the right column of Figure 2, by interpolating the values of number densities on the grid of the simulation domain. The number density characteristics of the regions, such as the solar wind (moderate), magnetosheath (high), and magnetosphere (low), are also revealed here.

The laser links sweep across the annulus formed by the inscribed circle and the circumcircle (red circle) of the detector's triangle as the satellites orbiting around the geocenter. We calculate the OPD noise Δl based on Equation (8) and the satellites' orbits. The integration of the number density along each laser beam shows spatial and temporal variations due to the changes of the positions and directions of the laser beams in the magnetosphere and the evolution of the geometrical shapes and the number densities of the structures. During one revolution of the satellites around the Earth, the time series of Δl of S1-S2 for $\varphi_s = 0^\circ, 30^\circ, 60^\circ, 90^\circ$ are shown in Figure 3. For $\varphi_s = 0^\circ$, the correlation coefficient between the time series of P_{dyn} and Δl is 0.83, which is about two to three times larger than the ones for $\varphi_s = 30^\circ$ (0.48), 60° (0.33), and 90° (0.28). For $\varphi_s = 30^\circ, 60^\circ, 90^\circ$, the amplitude of the OPD noise reaches 1.2 pm at the position when the laser beam passes through the magnetosheath on the dayside (around 300° in Figure 3), while Δl is only about 0.05 pm at the position where the laser beam passes through the magnetotail on the nightside (around 120° in Figure 3). These results indicate that the variation of Δl for $\varphi_s = 0^\circ$ is mainly due to the evolution of P_{dyn} in time, whereas the variations of Δl for $\varphi_s = 30^\circ, 60^\circ, 90^\circ$ are mainly due to the fact that the number density in the magnetosheath is much higher than that in the magnetotail.

4.2. OPD noise for single link and Michelson interferometer

Figure 4 shows the amplitude spectral densities (ASDs) of the time series of Δl for the single links. Here, we have used Savitzky-Golay filter (Savitzky & Golay 1964) to smooth the ASDs before fitting them by a single power law function. Note that the finest spatial resolution of the simulation is $0.25 R_E$ and the speed of TQ satellites is about 2 km s^{-1} , it takes each satellite about 800 s to move between two grid points. So that the ASDs of the OPD noise at range of $f > 1/800 \text{ Hz}$ can be underestimated. In fact, this underestimation has been shown in Figure 4, where there is a knee point at $f \approx 1/800 \text{ Hz}$ and the spectra become steeper when $f \gtrsim 1/800 \text{ Hz}$. Here, only the ASDs of the OPD noise at range of $f \lesssim 1/800 \text{ Hz}$ are used in the fitting of the spectral index. The best-fit spectral indices for $\varphi_s = 0^\circ, 30^\circ, 60^\circ$ and 90° , shown as the red dashed lines, are $-0.718, -0.577, -0.567$ and -0.588 , respectively. The corresponding spectral amplitudes at 1 mHz read $0.760, 0.651, 0.587$ and $0.573 \text{ pm}/\sqrt{\text{Hz}}$, respectively.

Michelson-type interferometer sketched in Figure 5a has been used as the fiducial data combination to study the science potential and data analysis for space-borne detectors (Feng et al. 2019; Wang et al. 2019; Liu et al. 2020; Huang et al. 2020). Its response and sensitivity to arbitrary incoming GWs for TQ have been studied in Hu et al. (2018). We denote the OPD noise that is produced during the propagation of the EW wave sent from spacecraft i and received by satellite j as Δl_{ij} (Prince et al. 2002). For a Michelson-type interferometer centered on S1, the OPD noise of two interferometer arms (S1–S2 and S1–S3) are $\Delta l_{12}, \Delta l_{21}, \Delta l_{13}$ and Δl_{31} . From Equation (8), $\Delta l_{12} = K/2f^2 \int_{S1}^{S2} N ds$, and similarly for $\Delta l_{21}, \Delta l_{13}$ and Δl_{31} . Since $\int_i^j N ds = \int_j^i N ds$, and the light propagation time between a pair of satellites ($\approx 0.6 \text{ s}$) is much less than the temporal resolution of our simulation (60 s), we set $\Delta l_{12} = \Delta l_{21}$ and $\Delta l_{13} = \Delta l_{31}$. Therefore, the OPD noise for a Michelson-type combinations can be written as follows,

$$\Delta l = 2(\Delta l_{12} - \Delta l_{13}). \quad (9)$$

From Equation (9), we can calculate the time series of Δl for a Michelson combination during one revolution of the satellites around the Earth. From Figure 6, we can see that the maxima of $|\Delta l|$ for the Michelson combination is about 3 pm . The typical amplitudes are magnified due to four combinations of the OPD noises of the single links.

Shown in Figure 7 are the ASDs of Δl for the Michelson interferometer for $\varphi_s = 0^\circ, 30^\circ, 60^\circ$, and 90° . Similarly, we fit the spectral profiles with power-law functions for the Michelson interferometer, which are shown as the red dashed lines in Figure 7. The best-fit spectral indices for $\varphi_s = 0^\circ, 30^\circ, 60^\circ$, and 90° are $-0.887, -0.544, -0.626$ and -0.683 . The corresponding spectral amplitudes at 1 mHz read $0.752, 1.167, 1.400$ and $1.512 \text{ pm}/\sqrt{\text{Hz}}$, respectively.

4.3. OPD noise for TDI combinations

In order to eliminate the otherwise overwhelming laser phase noise, the time delay interferometry (TDI) has been devised for the data processing of space-borne interferometric GW detectors (Armstrong et al. 1999; Estabrook et al. 2000; Tinto & Dhurandhar 2014). There are various data combinations for the TDI (Tinto & Dhurandhar 2014). In this work, we focus on the α and X data combinations, shown in Figure 5b and 5c, as the typical examples of the six-pulse and eight-pulse combinations of the first-generation TDI, respectively.

Consider the OPD noise accumulated along the laser propagation in space plasma, the phase fluctuation of the laser that is sent from satellite i and received by satellite j can be expressed as follows,

$$\Phi_{ij}(t) = \phi_{ij}(t) + h_{ij}(t) + n_{ij}(t) + s_{ij}(t), \quad (10)$$

where $\phi_{ij}(t)$ is the laser phase noise to be canceled by TDI, $h_{ij}(t)$ is the GW signal, and $n_{ij}(t)$ is the total nonlaser phase noise (Hellings 2001). $s_{ij}(t)$ is the phase noise associated with the OPD noise $\Delta l_{ij}(t)$,

$$s_{ij}(t) = 2\pi\Delta l_{ij}(t)/\lambda, \quad (11)$$

where $\lambda = 1064 \text{ nm}$ for the Nd:YAG laser used by TQ.

Set L_{ij} as the distance between satellites i and j and $c = 1$ hereafter, the total phase noise due to space plasma for the α combination, s_α , can be written as,

$$s_\alpha = s_{12}(t - L_{23} - L_{31}) + s_{23}(t - L_{31}) + s_{31}(t) - s_{13}(t - L_{32} - L_{21}) - s_{32}(t - L_{21}) - s_{21}(t). \quad (12)$$

Similarly, for the X combination, s_X can be written as,

$$s_X = s_{12}(t - L_{21} - L_{13} - L_{31}) + s_{21}(t - L_{13} - L_{31}) + s_{13}(t - L_{31}) + s_{31}(t) - s_{13}(t - L_{31} - L_{12} - L_{21}) - s_{31}(t - L_{12} - L_{21}) - s_{12}(t - L_{21}) - s_{21}(t). \quad (13)$$

For the nearly equilateral triangular constellation of TQ, $L_{ij} = L \approx 0.6$ s. Note that L is much smaller than the temporal resolution of the MHD simulation, $\Delta t = 60$ s. As mentioned in Section 4.2, $\int_j^t N ds = \int_i^j N ds$, so that $s_{ij}(t) = s_{ji}(t)$. Thus, s_α is reduced to

$$s_\alpha = s_{12}(t - 2L) + s_{31}(t) - s_{12}(t) - s_{31}(t - 2L). \quad (14)$$

And s_X is reduced to

$$s_X = s_{12}(t - 3L) + s_{12}(t - 2L) + s_{31}(t - L) + s_{31}(t) - s_{12}(t - L) - s_{12}(t) - s_{31}(t - 3L) - s_{31}(t - 2L). \quad (15)$$

As in the single link case, we can obtain $s_{ij}(t)$ for every 60 s. s_{ij} at delayed times can be obtained by linear interpolation, i.e., $s_{ij}(t - \delta t) = s_{ij}(t) + (s_{ij}(t - \Delta t) - s_{ij}(t))(\delta t/\Delta t)$. In this way, Equations (14) and (15) can be modified as follows,

$$s_\alpha = (s_{12}(t - \Delta t) - s_{12}(t))\frac{2L}{\Delta t} - (s_{31}(t - \Delta t) - s_{31}(t))\frac{2L}{\Delta t}, \quad (16)$$

$$s_X = 2s_\alpha. \quad (17)$$

From Equation (17), we can see that the OPD noise reduction for the α combination is a factor of two better than that for the X combination. This is because the laser beam will pass through one of the arms twice for the X combination, but only once for the α combination (see Figure 5). Combining Equations (11), (16), and (17), we can calculate the OPD noises for the α and X combinations as shown in Figure 8. The maxima of $|\Delta l|$ for the α and X combinations are about 0.004 and 0.008 pm, respectively, which are about two orders of magnitude smaller than that for the Michelson combination. This indicates that TDI can significantly suppress the common-mode OPD noise.

Figure 9 shows the ASDs of Δl for the α and X combinations. Similar to the single link and Michelson combination, the spectra of the ASDs become steeper when $f \gtrsim 1/800$ Hz. The best-fit spectral indices for the α (X) combination are 0.108, 0.399, 0.341, and 0.309 for $\varphi_s = 0^\circ, 30^\circ, 60^\circ,$ and 90° ; The corresponding spectral amplitudes at 1 mHz read 0.003 (0.005), 0.004 (0.008), 0.005 (0.010), and 0.005 (0.010) pm/ $\sqrt{\text{Hz}}$ at 1 mHz, respectively.

5. DISCUSSIONS

5.1. The impact of OPD noise on the sensitivity

The equivalent strain noise ASD ($\sqrt{S_n}$) for the Michelson combination (denoted as $\sqrt{S_n^M}$) is as follows (Hu et al. 2018),

$$S_n^M = S_n^x + S_n^a \left(1 + \frac{10^{-4} \text{ Hz}}{f}\right), \quad (18)$$

where $\sqrt{S_n^x}$ is the equivalent strain noise ASD of the displacement measurement, $\sqrt{S_n^a}$ is the equivalent strain noise due to residual acceleration. And the equivalent strain noise ASD for the α ($\sqrt{S_n^\alpha}$) and X ($\sqrt{S_n^X}$) combinations are as follows (Armstrong et al. 1999),

$$S_n^\alpha = [4\sin^2(3\pi fL/c) + 24\sin^2(\pi fL/c)]S_n^a + 6S_n^x, \quad (19)$$

$$S_n^X = [4\sin^2(4\pi fL/c) + 32\sin^2(2\pi fL/c)]S_n^a + 16\sin^2(2\pi fL/c)S_n^x, \quad (20)$$

In order to compare the OPD noises with TQ's equivalent strain noise ASDs for the Michelson ($\sqrt{S_n^M}$), α ($\sqrt{S_n^\alpha}$), and X ($\sqrt{S_n^X}$) combinations, we calculate the ASDs of the equivalent strains of the OPD noises as $\Delta l/L$ for the corresponding data combinations. Using the best-fit spectra of the OPD noises for the Michelson, α , and X combinations, we calculate the ratio between $(\Delta l/L)$ and $\sqrt{S_n^M}$, $\sqrt{S_n^\alpha}$, $\sqrt{S_n^X}$, and the results are shown in Figure 10.

For the Michelson combination, the maximum of $(\Delta l/L)/\sqrt{S_n^M}$ is about 0.29 at ≈ 10 mHz. $(\Delta l/L)/\sqrt{S_n^M}$ increases with increasing frequency f when $f \lesssim 10$ mHz. This is due to the fact that $\sqrt{S_n^a}$ is dominated, in this frequency range, by the acceleration noise with $\sqrt{S_n^a} \propto f^{-2}$, the spectral index of which is less than the ones of Δl for the Michelson combination. $(\Delta l/L)/\sqrt{S_n^M}$ decreases with f when $f \gtrsim 10$ mHz, and $(\Delta l/L)/\sqrt{S_n^M}$ decreases to about 0.04 at the transfer frequency $f_* \approx 0.3$ Hz (Hu et al. 2018). This is because $\sqrt{S_n^M}$ is dominated by the position noise which is approximately white in this frequency range.

For the TDI α combinations, $(\Delta l/L)/\sqrt{S_n^\alpha}$ at $f \approx 10$ mHz is about 0.005, which is about 1/60 of that for the Michelson combination. However, as the spectral index of Δl is slightly larger than 0 for α combinations, $(\Delta l/L)/\sqrt{S_n^\alpha}$ increase smoothly in the frequency range of $10^{-2} < f < 1$ Hz, and the maxima of $(\Delta l/L)/\sqrt{S_n^\alpha}$ from different φ_s are about 0.015 at the transfer frequency f_* , which is much lower than that for the Michelson combination. For the TDI X combinations, the maximum of $(\Delta l/L)/\sqrt{S_n^X}$ is about 0.12 at $f \approx 10$ mHz, and $(\Delta l/L)/\sqrt{S_n^X} \approx 0.02$ at the transfer frequency f_* , which is also much lower than that for the Michelson combination, but higher than that for the α combination. $(\Delta l/L)/\sqrt{S_n^X}$ decreases with f when $f \gtrsim 10$ mHz, this is because that the spectral index of $\sqrt{S_n^X}$ is larger than that of the Δl for X combination in the frequency range $f \gtrsim 10$ mHz. The results suggest that the TDI combinations, especially α type, can efficiently suppress the common-mode OPD noise produced during the laser propagation in space plasma for the most sensitive frequency range of TQ. However, due to the limited high frequency reach of our simulation, the results in Figure 10, which are obtained by extrapolating the red dashed lines in Figure 9, may overestimate or underestimate the OPD noises when $f \gtrsim 1/800$ Hz. Further investigation with higher spatial and temporal resolution is needed.

Since the spectral indices of the ASDs of the OPD noises for a single link and a Michelson combination are about -2/3, the OPD noise will be more significant in lower frequencies. And considering that LISA is more sensitive than TQ in lower frequencies ($f \lesssim 10$ mHz) (Babak et al. 2017; Feng et al. 2019), the ratios between $(\Delta l/L)$ and $\sqrt{S_n}$ of LISA in the lower frequencies for the single link will be larger than that of TQ. However, in practice, for LISA, TQ and other space-borne GWs detectors, one will use TDI data combinations which can suppress the otherwise dominating laser frequency noise, rather than single link data, in GW data analysis. Based on our results, TDI can partially cancel the common-mode OPD noise.

In addition, Figures 3, 6 and 8 show respectively that the OPD noises rooted from space plasma are strongly non-stationary for the single link, Michelson, and TDI combinations. However, as shown in Figure 10, the OPD noises, especially for the TDI combinations, are not dominating in the total noise budget. Therefore, it may not significantly change the anticipated overall statistical properties of the total noise. On the other hand, when the non-stationarity in the total noise is strong, identifying and addressing the non-stationary noise will become crucial in the GW data analysis (Mohanty 2000; Edwards et al. 2020). The non-stationarity in noise deserves careful consideration in the development of GW detectors.

5.2. Space weather

The solar wind dynamic pressure P_{dyn} is the most important parameter that determines the Earth magnetosphere's geometric structures and distributions of electron number density (Lu et al. 2015; Wang et al. 2016). The more strongly the magnetosphere is compressed by the solar wind, and the larger the number density will be (Lu et al. 2015), which leads to the larger amplitude of the OPD noise. From the OMNI data of the solar wind (King & Papitashvili 2005), we obtain P_{dyn} with the value of 2.0 ± 1.2 nPa during a total solar cycle from 1997 to 2019. In this work, the input $P_{\text{dyn}} = 2.1 \pm 0.7$ nPa, which is approximated to the mean value of P_{dyn} during the total solar cycle. Consider that both the period of P_{dyn} and solar magnetic cycle are about 22 years and TQ is proposed to launch at early 2030s, P_{dyn} that is obtained 22 years before the real operation is a good approximation. We get P_{dyn} data from 2008 to 2012 (about 22 years before the launch) on OMNI website, and find that the time when P_{dyn} is larger than 3 nPa and 5 nPa accounts for only about 5% and 1% of the total period. Besides, the Earth magnetosphere encounters the solar eruptions, e.g. interplanetary shocks and coronal mass ejections, P_{dyn} can reach or even exceed 5 nPa in these cases. The laser propagation noises in the cases of solar eruptions are expected in future works. Recently, the OPD noise of LISA was estimated based on the in-situ observations from the Wind spacecraft (Smetana 2020). In contrast to the in-situ observations, the MHD simulation with the input of real time solar wind data can provide the global structure of the space environment with spatial resolution along the laser beams, and it can be applied to the future investigations of laser propagation noise for the other space-borne GW detectors. Furthermore, the SWMF model that used in this work is an MHD model, only the physical processes at global and the MHD scales can be revealed. On the other hand, the plasma-scale physical processes, such as plasma waves and turbulences, cannot be revealed by the SWMF model. For the impact of plasma scale physical process on the OPD noise, the hybrid or particle-in-cell (PIC) simulations are needed.

Besides obtaining the TEC from MHD simulations, it is also possible to derive the TEC from real-time observations. In order to obtain the TEC along the laser propagation path, we can transmit signals with two frequencies to reduce Δl , the dual-frequency scheme has been used in the Compass system (Yang et al. 2011), the Gravity Recovery and

Climate Experiment (GRACE) and GRACE Follow-on (GRACE-FO) (Tapley et al. 2004; Landerer et al. 2020). For dual-frequency scheme, there are two general methods, one is differential group delay, the other is differential carrier phase. Differential group time delay measures the time delay difference of two EM waves with different frequencies, and differential carrier phase measures the phase difference of two EM waves with different frequencies. The accuracy of differential group delay method is lower than that of differential carrier phase, but it can measure the absolute value of TEC. For the next-generation space-borne GW detectors, e.g., DECIGO (Kawamura et al. 2011), the proposed strain sensitivity is about five orders of magnitude lower than that of TQ, and the difference of the electron density between the solar wind at 1 AU and that around the TQ orbit with a geocentric altitude of 10^5 km is generally no more than one order of magnitude. Thus, the laser propagation noise will become a dominating environmental noise for DECIGO, and the laser ranging scheme with the dual-frequency laser will become a necessity.

6. CONCLUSIONS

Dispersion can cause OPD noise when the laser beams propagate in space plasma. In this work, the Appleton-Hartree equation, the orbits of TQ satellites and the global magnetosphere simulation based on the SWMF are used to analyze the OPD noise Δl for TQ at four typical relative positions of the detector's planes with $\varphi_s = 0^\circ, 30^\circ, 60^\circ$, and 90° .

The maxima of $|\Delta l|$ for the single link and the Michelson combination are about 1 and 3 pm, respectively. The maxima of $|\Delta l|$ can be reduced to about 0.004 and 0.008 pm for the TDI combination α and X , respectively. Furthermore, we calculate the ratio between the equivalent strain of the OPD noise and the one proposed for TQ, i.e., $(\Delta l/L)/\sqrt{S_n^M}$, $(\Delta l/L)/\sqrt{S_n^\alpha}$, $(\Delta l/L)/\sqrt{S_n^X}$ for the Michelson, α , X combinations, respectively. We find that in the most sensitive frequency range of TQ, the TDI combinations can suppress the OPD noise significantly. For the next-generation space-borne GW detectors, transmitting EM waves with two frequencies can be considered as a necessity to significantly reduce the OPD noise.

ACKNOWLEDGMENTS

The simulations used in this work are provided by the Community Coordinated Modeling Center (CCMC) at Goddard Space Flight Center through their public Runs on the Request system. This work is carried out using the SWMF and BATSRUS tools developed at the University of Michigan's Center for Space Environment Modeling. S.W. is supported by National Key R & D Program of China (Grant 2020YFC2201201), the National Natural Science Foundation of China (NSFC) under grant 11803008. Y.W. is supported by NSFC under grants 11973024 and 11690021, and Guangdong Major Project of Basic and Applied Basic Research (Grant No. 2019B030302001). L.L.F. is supported by NSFC under grant 42004156. S.T. was supported by NASA grant 80NSSC17K0453. Z.Z.B. is supported by NSFC under grant 11727814 and 11975105. C.P.F. is supported by NSFC under grant 11961131002.

REFERENCES

- Abbott, B. P., Abbott, R., Abbott, T. D., et al. 2016, *Physical Review Letters*, 116, 061102, doi: [10.1103/PhysRevLett.116.061102](https://doi.org/10.1103/PhysRevLett.116.061102)
- . 2019, *Physical Review X*, 9, 031040, doi: [10.1103/PhysRevX.9.031040](https://doi.org/10.1103/PhysRevX.9.031040)
- Abbott, R., Abbott, T. D., Abraham, S., et al. 2020, arXiv e-prints, arXiv:2010.14527. <https://arxiv.org/abs/2010.14527>
- Allen, R. C., Zhang, J. C., Kistler, L. M., et al. 2015, *Journal of Geophysical Research (Space Physics)*, 120, 5574, doi: [10.1002/2015JA021333](https://doi.org/10.1002/2015JA021333)
- Amaro-Seoane, P., Audley, H., Babak, S., et al. 2017, arXiv e-prints. <https://arxiv.org/abs/1702.00786>
- Armano, M., Audley, H., Baird, J., et al. 2020, *Monthly Notices of the Royal Astronomical Society*, 494, 3014, doi: [10.1093/mnras/staa830](https://doi.org/10.1093/mnras/staa830)
- Armstrong, J. W., Estabrook, F. B., & Tinto, M. 1999, *ApJ*, 527, 814, doi: [10.1086/308110](https://doi.org/10.1086/308110)
- Babak, S., Gair, J., Sesana, A., et al. 2017, *Phys. Rev. D*, 95, 103012, doi: [10.1103/PhysRevD.95.103012](https://doi.org/10.1103/PhysRevD.95.103012)
- Bao, J., Shi, C., Wang, H., et al. 2019, *PhRvD*, 100, 084024, doi: [10.1103/PhysRevD.100.084024](https://doi.org/10.1103/PhysRevD.100.084024)
- Cutler, C., & Harms, J. 2006, *Physics*, 73, 1405
- Dimmock, A. P., & Nykyri, K. 2013, *Journal of Geophysical Research (Space Physics)*, 118, 4963, doi: [10.1002/jgra.50465](https://doi.org/10.1002/jgra.50465)

- Edwards, M. C., Maturana-Russel, P., Meyer, R., et al. 2020, *PhRvD*, 102, 084062, doi: [10.1103/PhysRevD.102.084062](https://doi.org/10.1103/PhysRevD.102.084062)
- Estabrook, F. B., Tinto, M., & Armstrong, J. W. 2000, *PhRvD*, 62, 042002, doi: [10.1103/PhysRevD.62.042002](https://doi.org/10.1103/PhysRevD.62.042002)
- Fan, H.-M., Hu, Y.-M., Barausse, E., et al. 2020, *Phys. Rev. D*, 102, 063016, doi: [10.1103/PhysRevD.102.063016](https://doi.org/10.1103/PhysRevD.102.063016)
- Feng, W.-F., Wang, H.-T., Hu, X.-C., Hu, Y.-M., & Wang, Y. 2019, *PhRvD*, 99, 123002, doi: [10.1103/PhysRevD.99.123002](https://doi.org/10.1103/PhysRevD.99.123002)
- Gong, X., Lau, Y.-K., Xu, S., et al. 2015, in *Journal of Physics Conference Series*, Vol. 610, *Journal of Physics Conference Series*, 012011, doi: [10.1088/1742-6596/610/1/012011](https://doi.org/10.1088/1742-6596/610/1/012011)
- Hanson, J., MacKeiser, G., Buchman, S., et al. 2003, *Classical and Quantum Gravity*, 20, S109, doi: [10.1088/0264-9381/20/10/313](https://doi.org/10.1088/0264-9381/20/10/313)
- Hasegawa, H., Fujimoto, M., Phan, T. D., et al. 2004, *Nature*, 430, 755, doi: [10.1038/nature02799](https://doi.org/10.1038/nature02799)
- He, J., Tu, C., Marsch, E., & Yao, S. 2012, *ApJL*, 745, L8, doi: [10.1088/2041-8205/745/1/L8](https://doi.org/10.1088/2041-8205/745/1/L8)
- Hellings, R. W. 2001, *PhRvD*, 64, 022002, doi: [10.1103/PhysRevD.64.022002](https://doi.org/10.1103/PhysRevD.64.022002)
- Hu, X.-C., Li, X.-H., Wang, Y., et al. 2018, *Classical and Quantum Gravity*, 35, 095008, doi: [10.1088/1361-6382/aab52f](https://doi.org/10.1088/1361-6382/aab52f)
- Huang, S.-J., Hu, Y.-M., Korol, V., et al. 2020, *Phys. Rev. D*, 102, 063021, doi: [10.1103/PhysRevD.102.063021](https://doi.org/10.1103/PhysRevD.102.063021)
- Huang, S. Y., Zhou, M., Sahraoui, F., et al. 2012, *Geophys. Res. Lett.*, 39, L11104, doi: [10.1029/2012GL052210](https://doi.org/10.1029/2012GL052210)
- Huang, S. Y., Sahraoui, F., Yuan, Z. G., et al. 2018, *ApJ*, 861, 29, doi: [10.3847/1538-4357/aac831](https://doi.org/10.3847/1538-4357/aac831)
- Hutchinson, I. H. 2002, *Principles of Plasma Diagnostics*
- Israel, G. L., Hummel, W., Covino, S., et al. 2002, *A&A*, 386, L13, doi: [10.1051/0004-6361:20020314](https://doi.org/10.1051/0004-6361:20020314)
- Kawamura, S., Ando, M., Seto, N., et al. 2011, *Classical and Quantum Gravity*, 28, 094011, doi: [10.1088/0264-9381/28/9/094011](https://doi.org/10.1088/0264-9381/28/9/094011)
- King, J. H., & Papitashvili, N. E. 2005, *Journal of Geophysical Research (Space Physics)*, 110, A02104, doi: [10.1029/2004JA010649](https://doi.org/10.1029/2004JA010649)
- Landerer, F. W., Flechtner, F. M., Save, H., et al. 2020, *Geophys. Res. Lett.*, 47, e88306, doi: [10.1029/2020GL088306](https://doi.org/10.1029/2020GL088306)
- Liu, S., Hu, Y.-M., Zhang, J.-d., & Mei, J. 2020, *Phys. Rev. D*, 101, 103027, doi: [10.1103/PhysRevD.101.103027](https://doi.org/10.1103/PhysRevD.101.103027)
- Lu, J. Y., Wang, M., Kabin, K., et al. 2015, *Planet. Space Sci.*, 106, 108, doi: [10.1016/j.pss.2014.12.003](https://doi.org/10.1016/j.pss.2014.12.003)
- Lu, L., Liu, Y., Duan, H., Jiang, Y., & Yeh, H.-C. 2020, *Plasma Science and Technology*, 22, 115301, doi: [10.1088/2058-6272/abab69](https://doi.org/10.1088/2058-6272/abab69)
- Lu, L.-F., Su, W., Zhang, X., et al. 2021, *Journal of Geophysical Research: Space Physics*, 126, e2020JA028579, doi: <https://doi.org/10.1029/2020JA028579>
- Luo, J., Chen, L.-S., Duan, H.-Z., et al. 2016, *Classical and Quantum Gravity*, 33, 035010, doi: [10.1088/0264-9381/33/3/035010](https://doi.org/10.1088/0264-9381/33/3/035010)
- Luo, J., Bai, Y.-Z., Cai, L., et al. 2020, *Classical and Quantum Gravity*, 37, 185013, doi: [10.1088/1361-6382/aba66a](https://doi.org/10.1088/1361-6382/aba66a)
- Mei, J., Bai, Y.-Z., Bao, J., et al. 2020, *Progress of Theoretical and Experimental Physics*, doi: [10.1093/ptep/ptaa114](https://doi.org/10.1093/ptep/ptaa114)
- Mohanty, S. D. 2000, *PhRvD*, 61, 122002, doi: [10.1103/PhysRevD.61.122002](https://doi.org/10.1103/PhysRevD.61.122002)
- Ni, W. T. 1998, in *Pacific Conference on Gravitation and Cosmology*, ed. Y. M. Cho, C. H. Lee, & S.-W. Kim, 309
- Prince, T. A., Tinto, M., Larson, S. L., & Armstrong, J. W. 2002, *PhRvD*, 66, 122002, doi: [10.1103/PhysRevD.66.122002](https://doi.org/10.1103/PhysRevD.66.122002)
- Sahraoui, F., Huang, S. Y., Belmont, G., et al. 2013, *ApJ*, 777, 15, doi: [10.1088/0004-637X/777/1/15](https://doi.org/10.1088/0004-637X/777/1/15)
- Savitzky, A., & Golay, M. J. E. 1964, *Analytical Chemistry*, 36, 1627
- Schumaker, B. L. 2003, *Classical and Quantum Gravity*, 20, S239, doi: [10.1088/0264-9381/20/10/327](https://doi.org/10.1088/0264-9381/20/10/327)
- Shi, C., Bao, J., Wang, H.-T., et al. 2019, *PhRvD*, 100, 044036, doi: [10.1103/PhysRevD.100.044036](https://doi.org/10.1103/PhysRevD.100.044036)
- Smetana, A. 2020, *MNRAS*, 499, L77, doi: [10.1093/mnras/laaa155](https://doi.org/10.1093/mnras/laaa155)
- Somiya, K. 2012, *Classical and Quantum Gravity*, 29, 124007, doi: [10.1088/0264-9381/29/12/124007](https://doi.org/10.1088/0264-9381/29/12/124007)
- Soucek, J., Escoubet, C. P., & Grison, B. 2015, *Journal of Geophysical Research (Space Physics)*, 120, 2838, doi: [10.1002/2015JA021087](https://doi.org/10.1002/2015JA021087)
- Stone, E. C., Frandsen, A. M., Mewaldt, R. A., et al. 1998, *SSRv*, 86, 1, doi: [10.1023/A:1005082526237](https://doi.org/10.1023/A:1005082526237)
- Su, W., Cheng, X., Ding, M. D., et al. 2016, *ApJ*, 830, 70, doi: [10.3847/0004-637X/830/2/70](https://doi.org/10.3847/0004-637X/830/2/70)
- Su, W., Cheng, X., Ding, M. D., Chen, P. F., & Sun, J. Q. 2015, *ApJ*, 804, 88, doi: [10.1088/0004-637X/804/2/88](https://doi.org/10.1088/0004-637X/804/2/88)
- Su, W., Wang, Y., Zhou, Z.-B., et al. 2020, *Classical and Quantum Gravity*, 37, 185017, doi: [10.1088/1361-6382/aba181](https://doi.org/10.1088/1361-6382/aba181)
- Takahashi, N., Seki, K., Teramoto, M., et al. 2018, *Geophys. Res. Lett.*, 45, 9390, doi: [10.1029/2018GL078857](https://doi.org/10.1029/2018GL078857)

- Tan, Z., Ye, B., & Zhang, X. 2020, *International Journal of Modern Physics D*, 29, 2050056, doi: [10.1142/S021827182050056X](https://doi.org/10.1142/S021827182050056X)
- Tapley, B. D., Bettadpur, S., Ries, J. C., Thompson, P. F., & Watkins, M. M. 2004, *Science*, 305, 503, doi: [10.1126/science.1099192](https://doi.org/10.1126/science.1099192)
- Tinto, M., Debra, D., Buchman, S., & Tilley, S. 2015, *Review of Scientific Instruments*, 86, 330
- Tinto, M., & Dhurandhar, S. V. 2014, *Living Reviews in Relativity*, 17, 6, doi: [10.12942/lrr-2014-6](https://doi.org/10.12942/lrr-2014-6)
- Tóth, G., Sokolov, I. V., Gombosi, T. I., et al. 2005, *Journal of Geophysical Research (Space Physics)*, 110, A12226, doi: [10.1029/2005JA011126](https://doi.org/10.1029/2005JA011126)
- Wang, H.-T., Jiang, Z., Sesana, A., et al. 2019, *PhRvD*, 100, 043003, doi: [10.1103/PhysRevD.100.043003](https://doi.org/10.1103/PhysRevD.100.043003)
- Wang, M., Lu, J. Y., Kabin, K., et al. 2018, *Journal of Geophysical Research (Space Physics)*, 123, 1915, doi: [10.1002/2017JA024750](https://doi.org/10.1002/2017JA024750)
- . 2016, *Journal of Geophysical Research (Space Physics)*, 121, 11,077, doi: [10.1002/2016JA022830](https://doi.org/10.1002/2016JA022830)
- Welling, D. T., & Ridley, A. J. 2010, *Space Weather*, 8, 03002, doi: [10.1029/2009SW000494](https://doi.org/10.1029/2009SW000494)
- Yang, F., Bai, Y., Hong, W., et al. 2020, *Classical and Quantum Gravity*, 37, 115005, doi: [10.1088/1361-6382/ab8489](https://doi.org/10.1088/1361-6382/ab8489)
- Yang, Y., Li, J., Xu, J., et al. 2011, *Chinese Science Bulletin*, 56, 2813, doi: [10.1007/s11434-011-4627-4](https://doi.org/10.1007/s11434-011-4627-4)
- Ye, B.-B., Zhang, X., Zhou, M.-Y., et al. 2019, *International Journal of Modern Physics D*, 28, 1950121, doi: [10.1142/S0218271819501219](https://doi.org/10.1142/S0218271819501219)
- Zhang, J., Liemohn, M. W., de Zeeuw, D. L., et al. 2007, *Journal of Geophysical Research (Space Physics)*, 112, A04208, doi: [10.1029/2006JA011846](https://doi.org/10.1029/2006JA011846)
- Zhao, J. S., Voitenko, Y., Yu, M. Y., Lu, J. Y., & Wu, D. J. 2014, *ApJ*, 793, 107, doi: [10.1088/0004-637X/793/2/107](https://doi.org/10.1088/0004-637X/793/2/107)
- Zhou, M., Deng, X. H., Zhong, Z. H., et al. 2019, *ApJ*, 870, 34, doi: [10.3847/1538-4357/aaf16f](https://doi.org/10.3847/1538-4357/aaf16f)

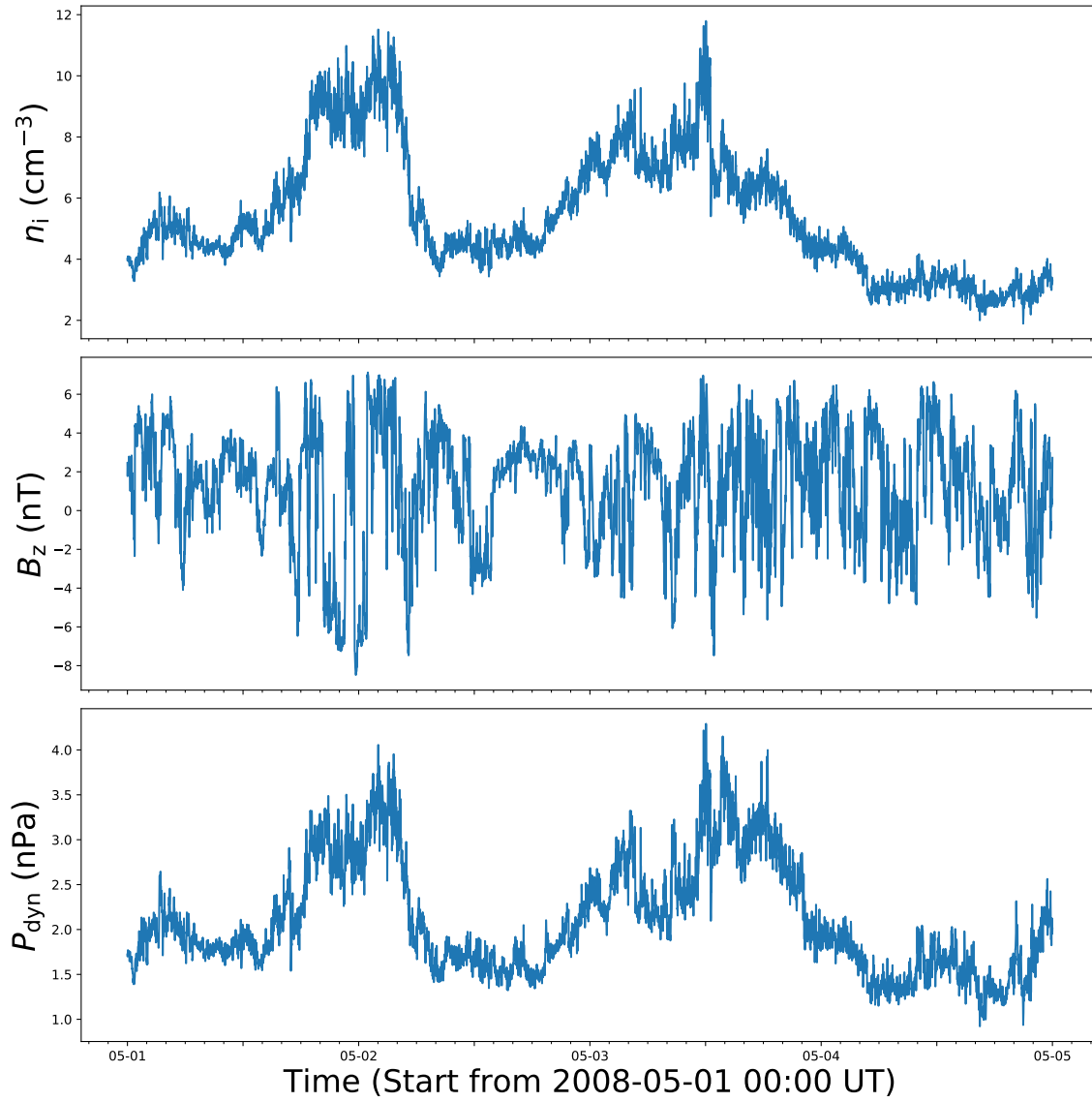


Figure 1. The input parameters observed by the ACE spacecraft which include the ion number density n_i (top panel), the space magnetic field B_z in the GSM coordinate (middle panel). The solar wind dynamic pressure P_{dyn} (bottom panel) is derived from the observations of the ACE.

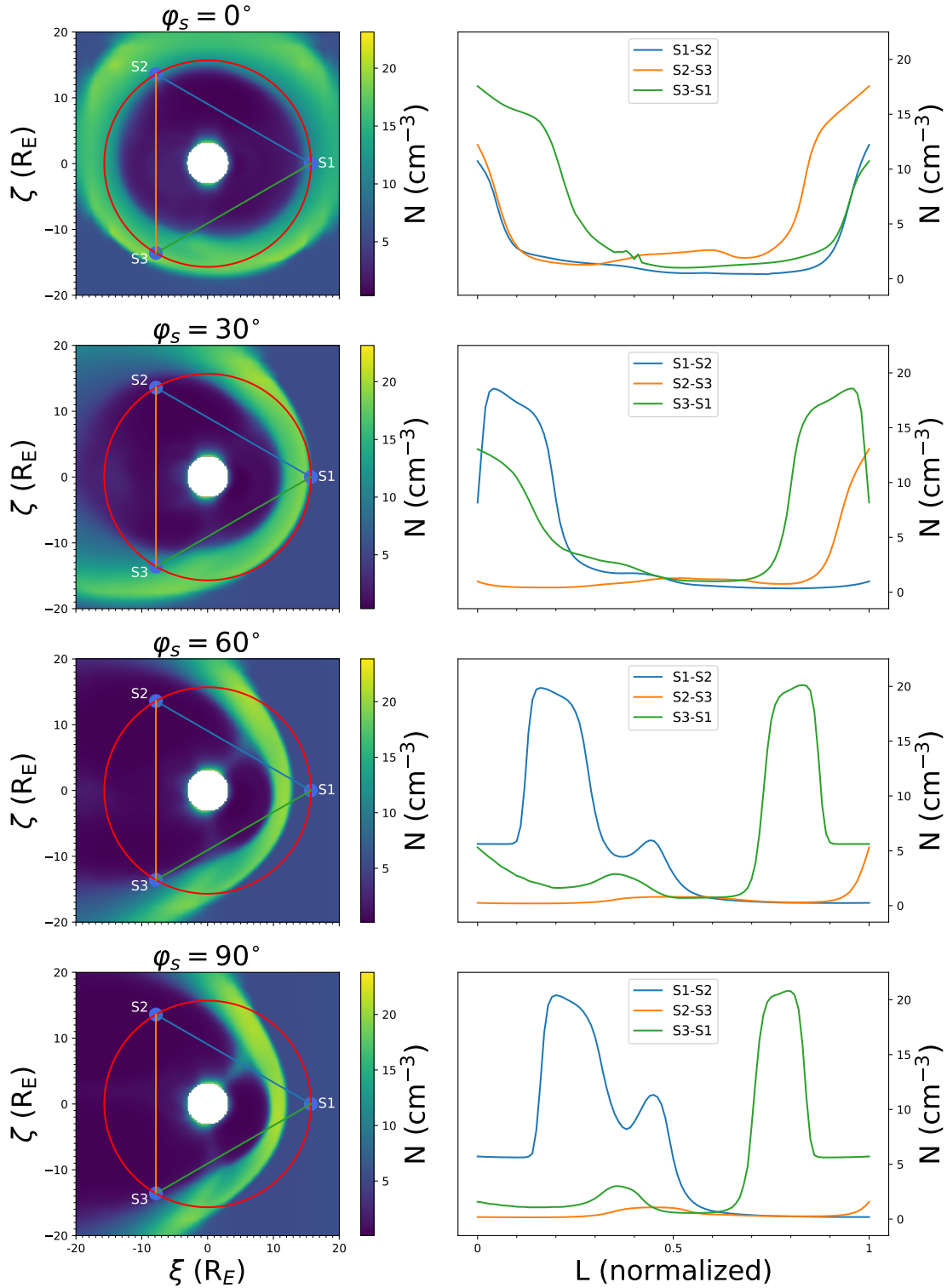


Figure 2. The left column displays the electron number density distributions (color scale) on the orbit planes with $\varphi_s = 0^\circ, 30^\circ, 60^\circ, 90^\circ$. ξ is the intersection line between the orbit plane and the ecliptic, ζ is perpendicular to the ecliptic, the red circle is the orbit of TQ's satellites. The laser link S1 – S2, S2 – S3, and S3 – S1 are represented by blue, orange, and green lines, respectively. The right panels are the distributions of the electron number densities along these three laser beams. Different colors correspond to the laser beams with the same colors in the left column.

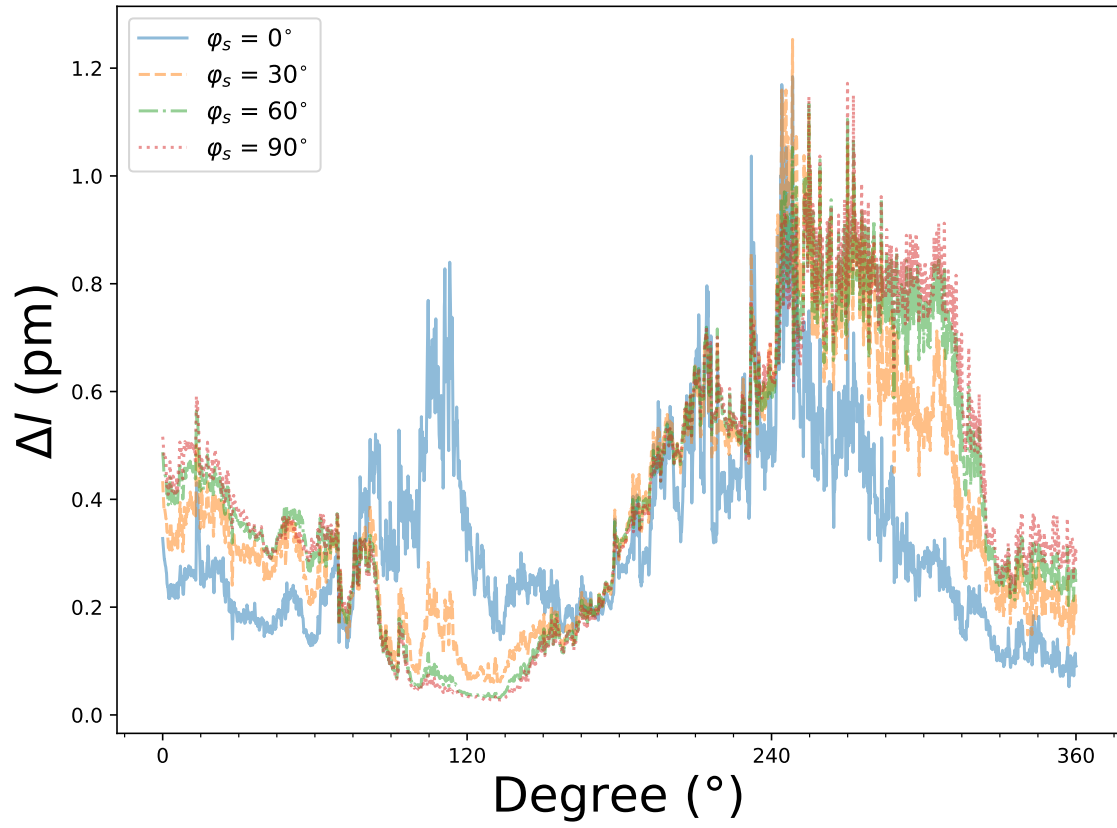


Figure 3. The OPD noises for a single link during a 3.65-day full-period orbit around the Earth on the orbit planes with $\varphi_s = 0^{\circ}, 30^{\circ}, 60^{\circ},$ and 90° .

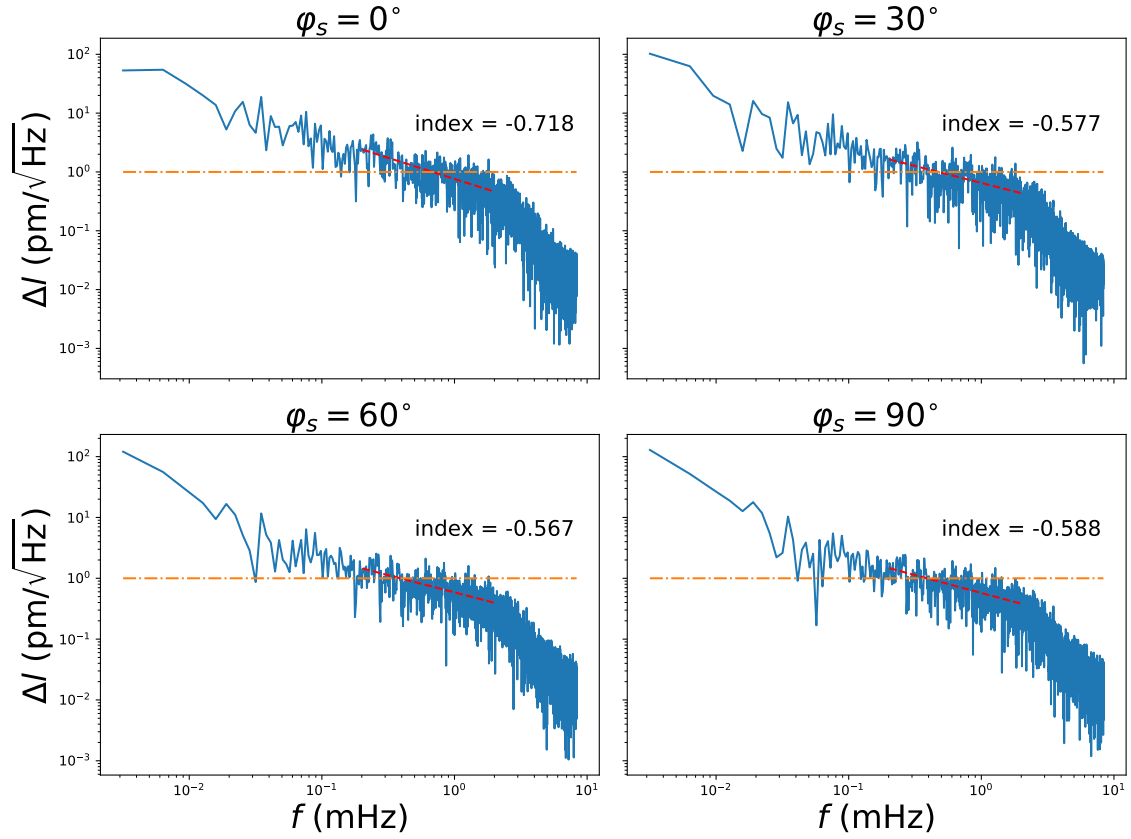


Figure 4. The ASDs of the OPD noises for a single link on the orbit planes with $\varphi_s = 0^\circ, 30^\circ, 60^\circ,$ and 90° . The orange dashed line is the proposed displacement measurement accuracy of TQ ($1 \text{ pm}/\sqrt{\text{Hz}}$) (Luo et al. 2016). Red dashed lines are the best-fit spectra of the ASDs.

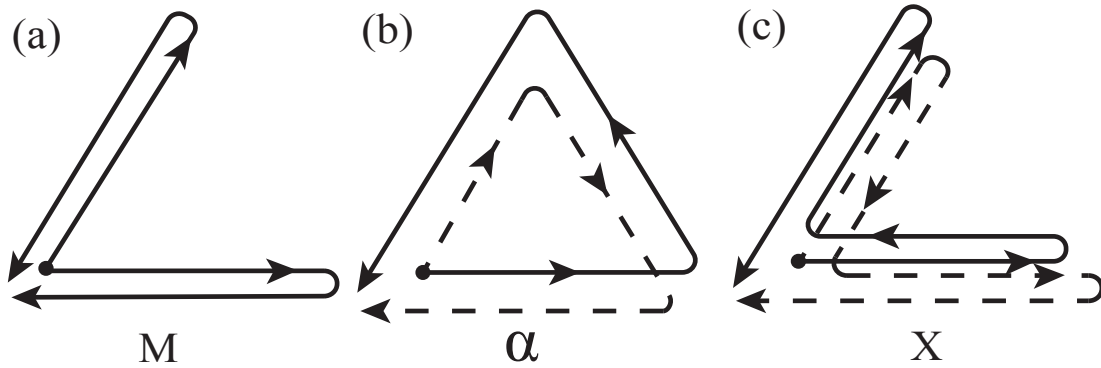


Figure 5. Schematic diagrams of Michelson, α , and X combinations.

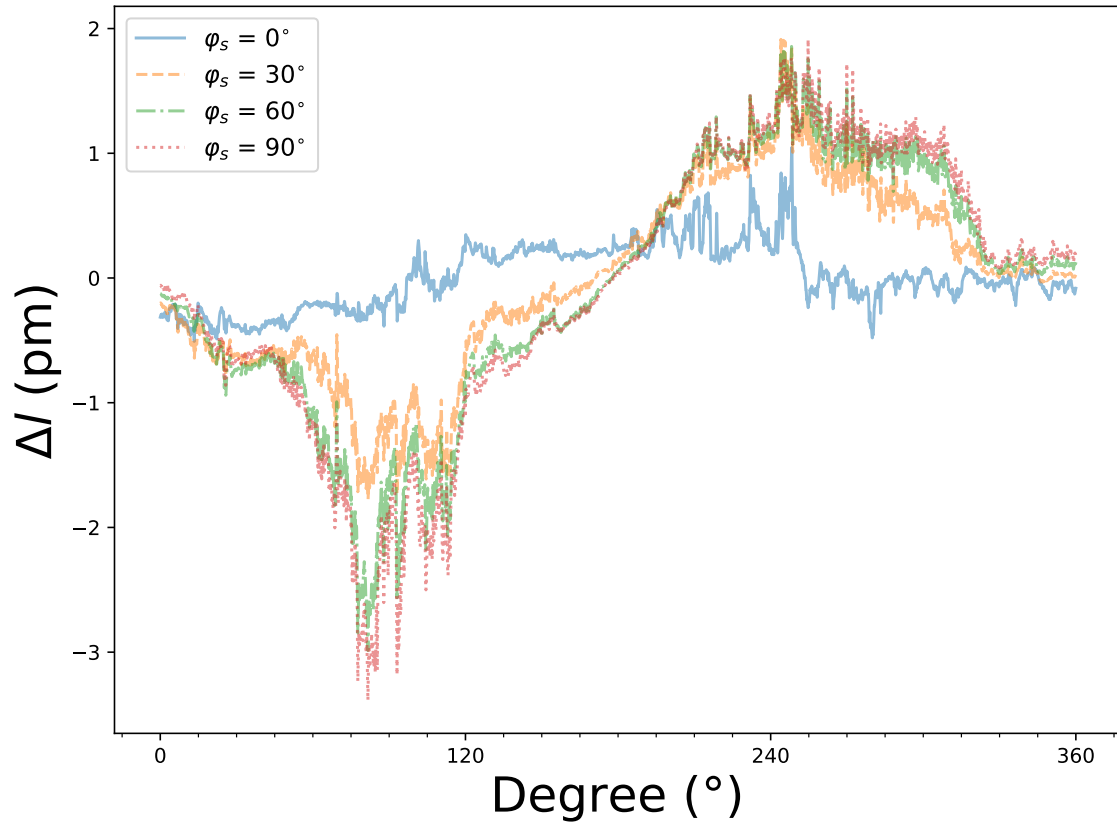


Figure 6. The OPD noises for a Michelson combination during a 3.65-day full-period orbit around the Earth. The blue, orange, green, and red curves are the OPD noises on the detector's planes with $\varphi_s = 0^{\circ}, 30^{\circ}, 60^{\circ}$, and 90° .

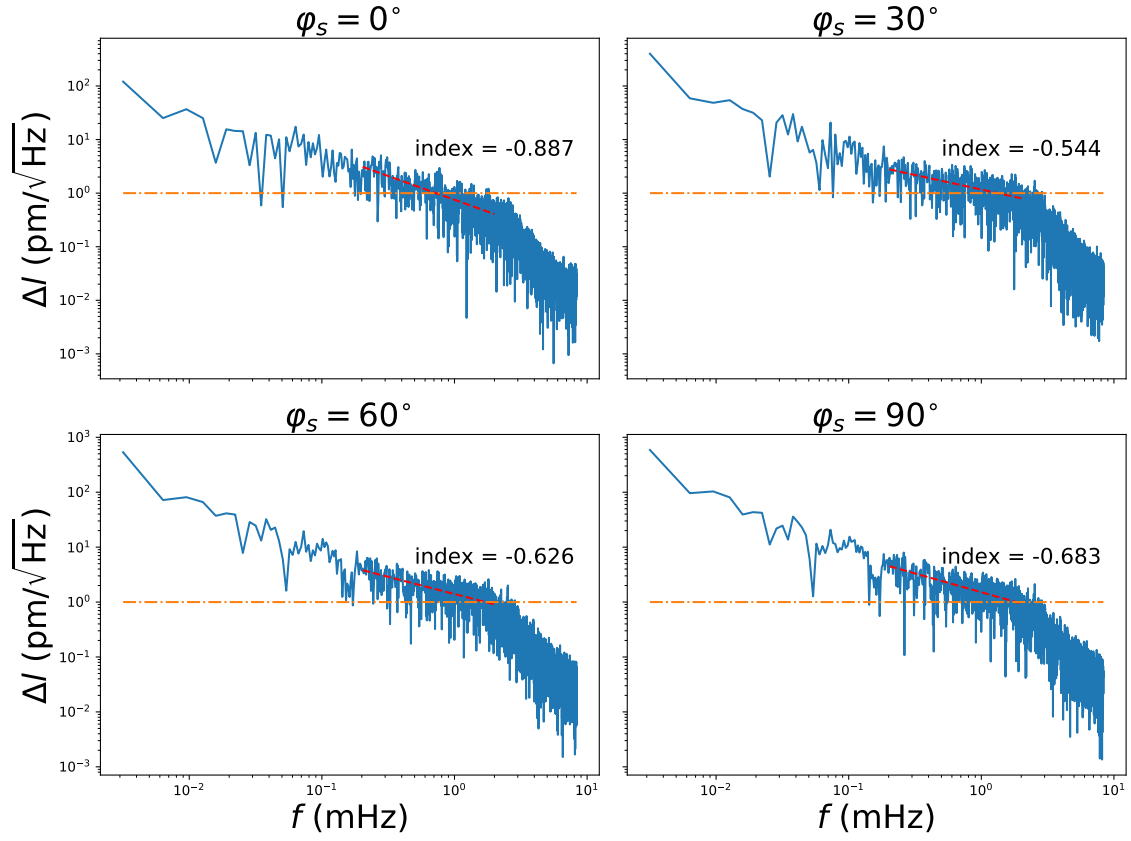


Figure 7. The ASDs of the OPD noises for the Michelson combination on the orbit planes with $\varphi_s = 0^\circ$, 30° , 60° , and 90° . The orange dashed line is the proposed displacement measurement accuracy of TQ (1 pm/ $\sqrt{\text{Hz}}$) (Luo et al. 2016). Red dashed lines are the best-fit spectra of the ASDs.

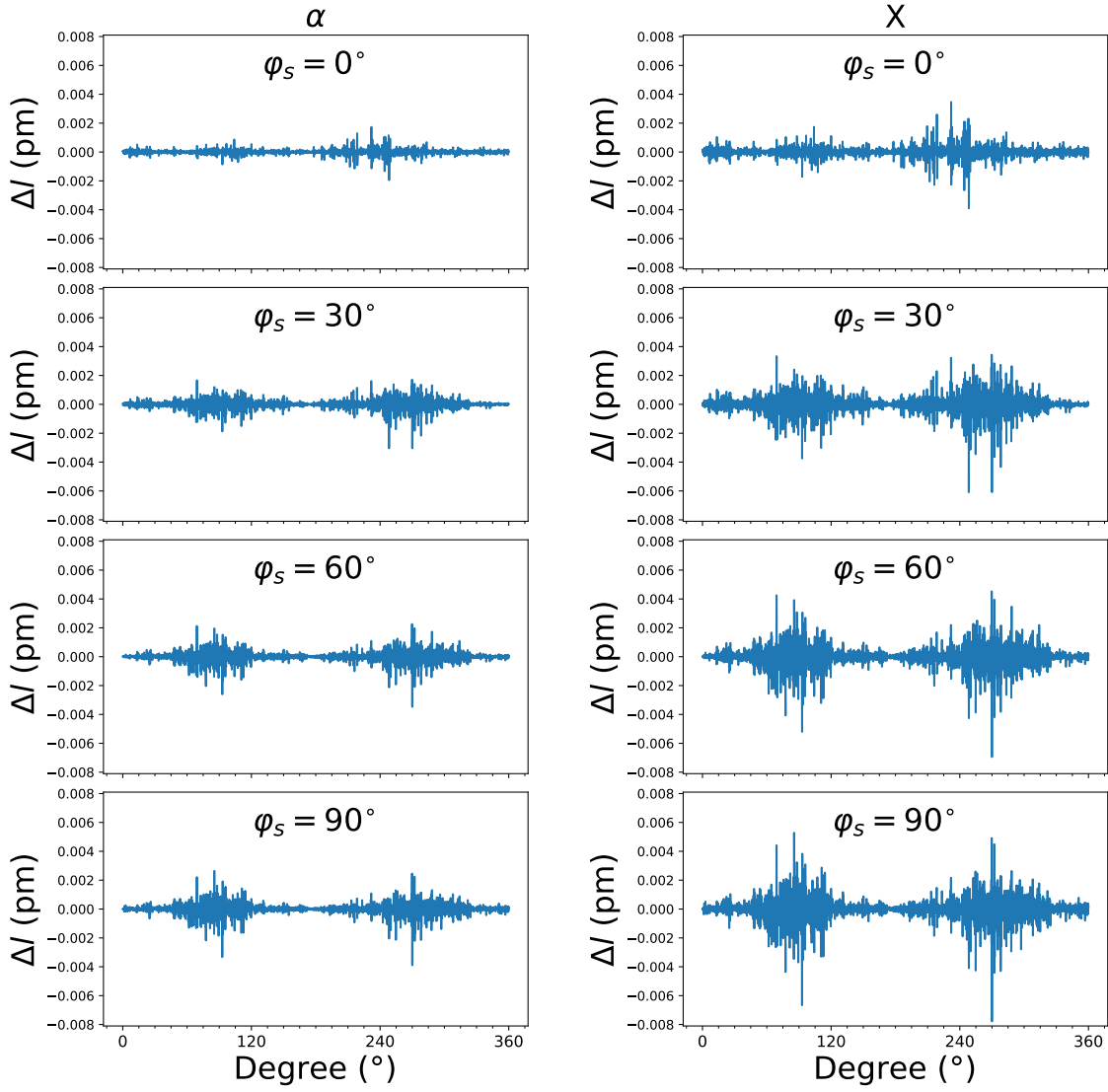


Figure 8. The OPD noises distributions for the α (left column) and X (right column) combinations on the orbit planes with $\varphi_s = 0^\circ, 30^\circ, 60^\circ, \text{ and } 90^\circ$.

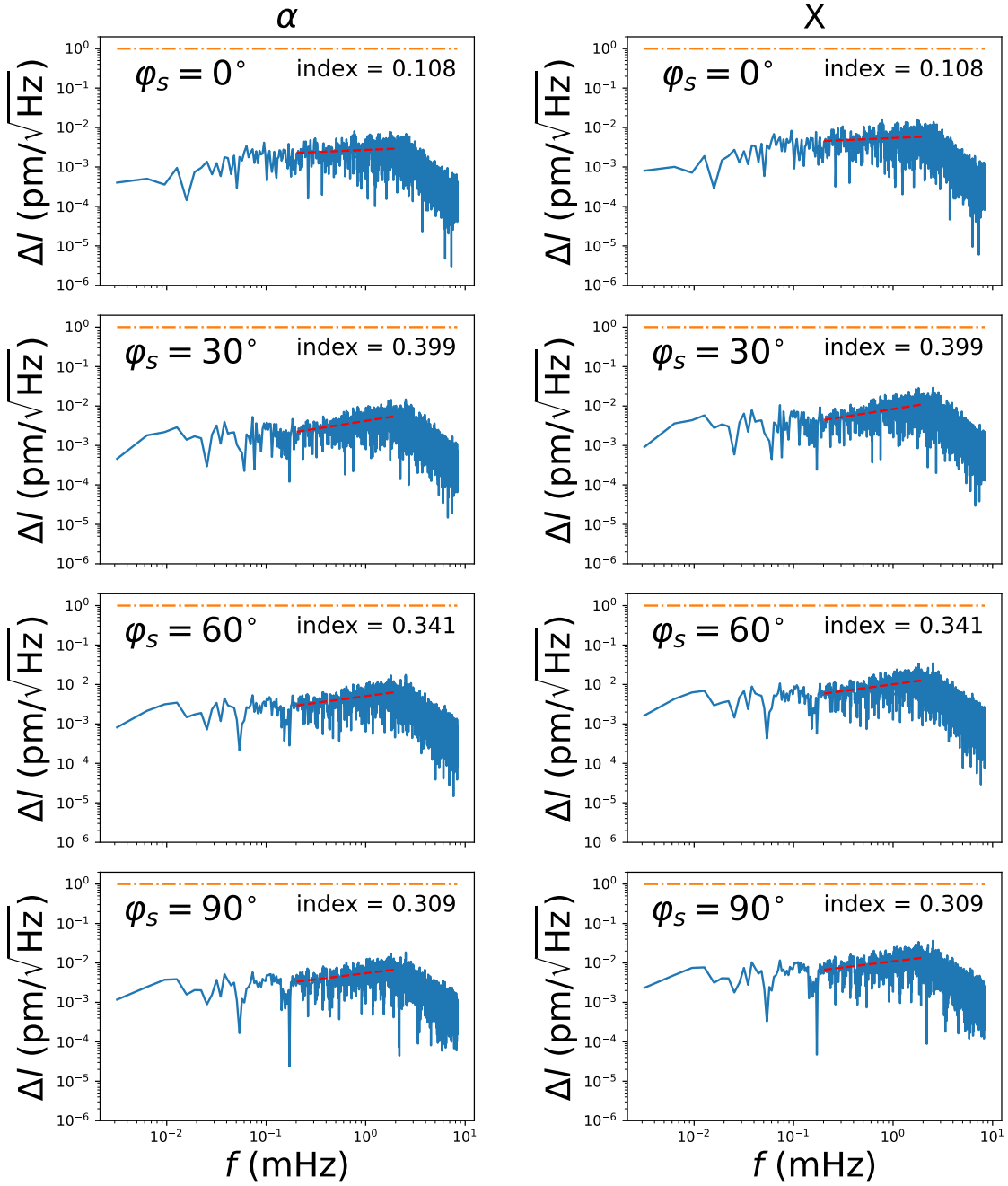


Figure 9. The ASDs of the OPD noises for the α (left column) and X (right column) combinations on the orbit planes with $\varphi_s = 0^\circ, 30^\circ, 60^\circ,$ and 90° . The orange dashed line is the proposed displacement measurement accuracy of TQ ($1 \text{ pm}/\sqrt{\text{Hz}}$) (Luo et al. 2016). Red dashed lines are the best-fit spectra of the ASDs.

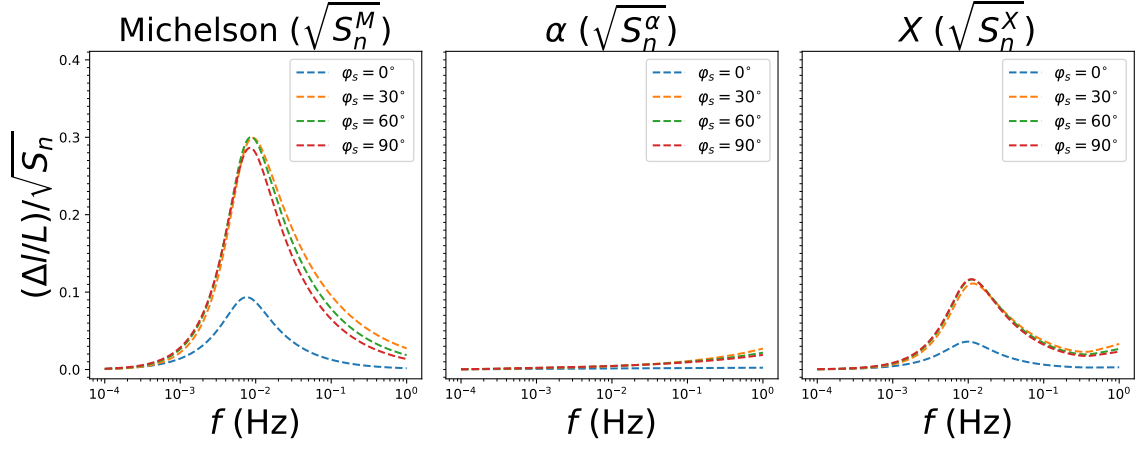


Figure 10. The ratios between the equivalent strain of the OPD noises and that of TQ $\sqrt{S_n}$, i.e., $(\Delta l/L)/\sqrt{S_n^M}$ for the Michelson combination (left panel), $(\Delta l/L)/\sqrt{S_n^\alpha}$ for the TDI α combination (middle panel), and $(\Delta l/L)/\sqrt{S_n^X}$ for the TDI X combination (right panel) on the orbit planes with $\varphi_s = 0^\circ, 30^\circ, 60^\circ,$ and 90° .